Characterization of the edge states in colloidal Bi$_2$Se$_3$ platelets

*Jesper R. Moes[1]†, Jara F. Vliem[1]†, Pedro M. M. C. de Melo[1], Thomas C. Wigmans, Andrés R. Botello-Méndez[1], Rafael G. Mendes[1], Ella F. van Brenk, Ingmar Swart[1], Lucas Maisel Licerán[2], Henk T. C. Stoof[2], Christophe Delerue[3], Zeila Zanolli[1], *Daniel Vanmaekelbergh[1]*

[1]Debye Institute for Nanomaterials Science, Utrecht University, Princetonplein 1, 3584 CC Utrecht, The Netherlands

[2] Institute for Theoretical Physics and Center for Extreme Matter and Emergent Phenomena, Utrecht University, Princetonplein 5, 3584 CC, Utrecht, The Netherlands

[3]Univ. Lille, CNRS, Univ. Polytechnique Hauts-de-France, Junia, UMR 8520 - IEMN, F-59000 Lille, France.

ABSTRACT.

The remarkable development of colloidal nanocrystals with controlled dimensions and surface chemistry has resulted in vast opto-electronic applications. But can they also form a platform for quantum materials, in which electronic coherence is key? Here, we use colloidal, two-dimensional Bi_2Se_3 crystals, with precise and uniform thickness and finite lateral dimensions in the 100 nm range, to study the evolution of a topological insulator from three to two dimensions. For a thickness of 4-6 quintuple layers, scanning tunneling spectroscopy shows an 8 nm wide, non-scattering state encircling the platelet. We discuss the nature of this edge state with a low-energy continuum model and ab-initio GW-Tight Binding theory. Our results also provide an indication for the maximum density of such states on a device.

Keywords: Edge State, Bismuth selenide nanoplatelets, Scanning tunneling spectroscopy, Topological insulator, Density functional theory, Quantum Spin Hall insulator

TEXT

In the last three decades, the field of colloidal nanocrystals has witnessed a remarkable development towards a versatile platform, offering nanocrystals of various chemical families with controlled shape, size, and surface chemistry(*1-3*). Today, brightly emitting semiconductor nanocrystals are successfully applied in the opto-electronic industry(*4-7*). Their success urges the question if colloidal nanocrystals could be of use for even more demanding purposes related to the emerging field of quantum materials, where coherence of electronic states is the main focus.

In two-dimensional (2D) quantum spin Hall insulators (QSHIs), the interior of the material is insulating, with a spin-orbit driven inversion of the valence and conduction bands. Due to the bulk-boundary correspondence, this results in a protected state at the edge of the 2D crystal with spin-momentum locking, crossing the inverted gap[8,9]. The helicity impedes backscattering from lattice vibrations and non-magnetic impurities. Therefore, QSHIs may form the basis for non-dissipative information transfer devices with a considerable reduction of energy consumption. Moreover, a QSHI can be converted into a topological superconductor by proximity engineering[10-13]. Such superconductors are of high scientific interest for advanced quantum computing[10,14,15].

Bulk, three-dimensional Bi_2Se_3, is a well-known topological insulator[16-19] with a large inverted gap of 200-300 meV and 2D Dirac-cone surface states that have been fully characterized with Angle-Resolved Photo-Emission Spectroscopy (ARPES)[16]. Bi_2Se_3 is a layered material with an integer number of quintuple layers (QLs, see Fig. 1), stacked with weak van der Waals interactions. But what happens if the thickness of the layered Bi_2Se_3 crystal is reduced to a small number (1-6) of QLs: does the three-dimensional topological insulator transform into a two-dimensional quantum spin Hall insulator, with helical quantum channels at the border of the crystal? This question is not only relevant from a purely scientific perspective, but also for applications, as electrical devices with a scalable density of quantum channels will require crystals of precise thickness and lateral dimensions. A first indication is given by the 4-band $k \cdot p$ model and ab-initio simulations of ref. *20*, predicting that 2D Bi_2Se_3 crystals with a reduced thickness ($\leq$ 7 QLs) are topologically non-trivial and should therefore have a one-dimensional, helical quantum state (with a predicted width of roughly 5 nm) at the crystal edge. Moreover, ARPES results on laterally extended crystals of 1-6 QLs in thickness show that the topological surface states of the

top and bottom become gapped due to hybridization($18,21,22$), indicating the transition from three to two dimensions. However, the presence and character of quantum channels that may reside at the edges of finite-sized 2D crystals has not been addressed experimentally.

Here, we use the virtues of colloidal chemistry to prepare 2D Bi_2Se_3 crystals with lateral dimensions in the 100 nm range and a uniform thickness of 1-6 QLs. These nanoplatelets (NPLs) can be expected to be strain-free, in contrast to larger crystals grown on a substrate(23). The limited dimensions of the platelets allow us to examine the crystal edges with scanning tunneling microscopy and spectroscopy (STM/STS). For each NPL, we measure the lateral dimensions, thickness, and the density of states DOS (E, x, y) of the interior region and the edge. We find that edge states are absent for ultrathin (i.e. 1-3 QLs) platelets, while we observe an 8-10 nm wide channel at the perimeter of 4-6 QL crystals, with enhanced density-of-states over an energy region of several hundreds of meV, indicative of the quantum spin Hall effect. We have examined the nature of the edge states with a low-energy eight-band $\boldsymbol{k \cdot p}$ model and first-principles GW calculations (GW-TB), from which we find evidence that the observed edge state may be a genuine helical quantum channel. Both models predict that the channels have a localization width in the 10 nm range, except very close to the Dirac point. These results indicate how close one-dimensional quantum channels can be positioned in devices.

Bi_2Se_3 nanoplatelets were synthesized according to a procedure adapted from *ref. 24* that we have optimized to obtain highly crystalline platelets of relatively small lateral size (see SI, Materials and Methods). As shown in Fig. 1A, the Bi_2Se_3 platelets have a hexagonal shape, uniform thickness, and a diameter of 166 ± 41 nm (Fig. 1A,B and fig. S1A). Fig. 1B shows a HAADF-STEM image of two NPLs of 3 and 4 quintuple layers (QLs) in the lateral viewing

direction. The Bi layers (white atoms in inset) can be observed as high-intensity lines. Figs. 1C and D confirm the crystalline quality of the Bi_2Se_3 nanoplatelets, and (STEM)-EDX measurements confirm the formation of Bi_2Se_3 (fig. S2). The thickness of the NPLs was determined with atomic force microscopy (AFM). As a single QL is 0.96 nm thick[25], the results indicate that most NPLs consist of 5-6 QLs (fig. S1B). We also prepared ultrathin (1-3 QLs) NPLs as shown in fig. S3.

Prior to STM/STS measurements, the NPL samples were treated to remove surfactants and organic contaminants as detailed in the supplementary information. Subsequently, the platelets were cast on Au/Mica substrates and inserted in the scanning tunneling microscope in UHV. Before measuring, the samples were annealed at 393 K for two hours to remove any residual organic contamination. Then, the sample was cooled to 4.5 K for UHV cryogenic scanning tunneling microscopy and spectroscopy. To investigate the effect of annealing on the nanocrystals, high resolution TEM was performed (see supplementary text and fig. S4). After annealing, we observed that Bi_2Se_3 material had been removed locally, which results in inclinations at the edges over a few nanometers. The results below show that the imperfections at the edge do not affect the interior band structure, nor the quality of the edge state.
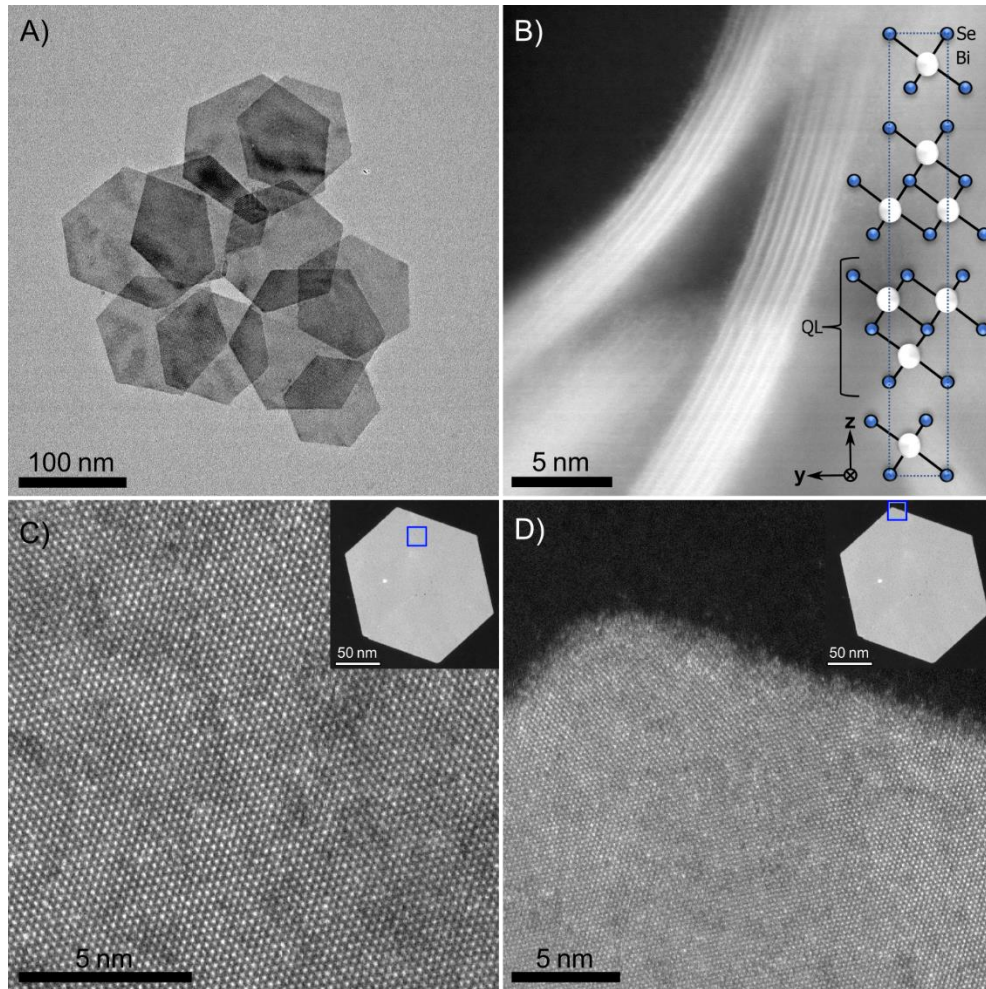
Figure 1. Structural characterization of colloidal Bi$_2$Se$_3$ NPLs.

(**A**) TEM image of an ensemble of typical Bi$_2$Se$_3$ NPLs. (**B**) HAADF-STEM image with the viewing direction along the NPL, showing two NPLs with 3 and 4 QLs, respectively. The two high intensity lines in each QL are due to the Bi columns (see inset). (**C,D**) High resolution HAADF-STEM images showing the high crystalline quality of the NPLs. The blue squares in the insets show the location at which the images were obtained.

We have investigated the electronic band structure of hexagonal Bi$_2$Se$_3$ platelets of 1-6 QLs in thickness by measuring the local DOS(E,x,y). For each Bi$_2$Se$_3$ platelet, the number of QLs can be retrieved by measuring the nominal height of the crystal at constant tunneling current. The results

are presented in the SI (figs. S5-S9). Here, we focus on a platelet with a thickness of 4 QLs, see Fig. 2.
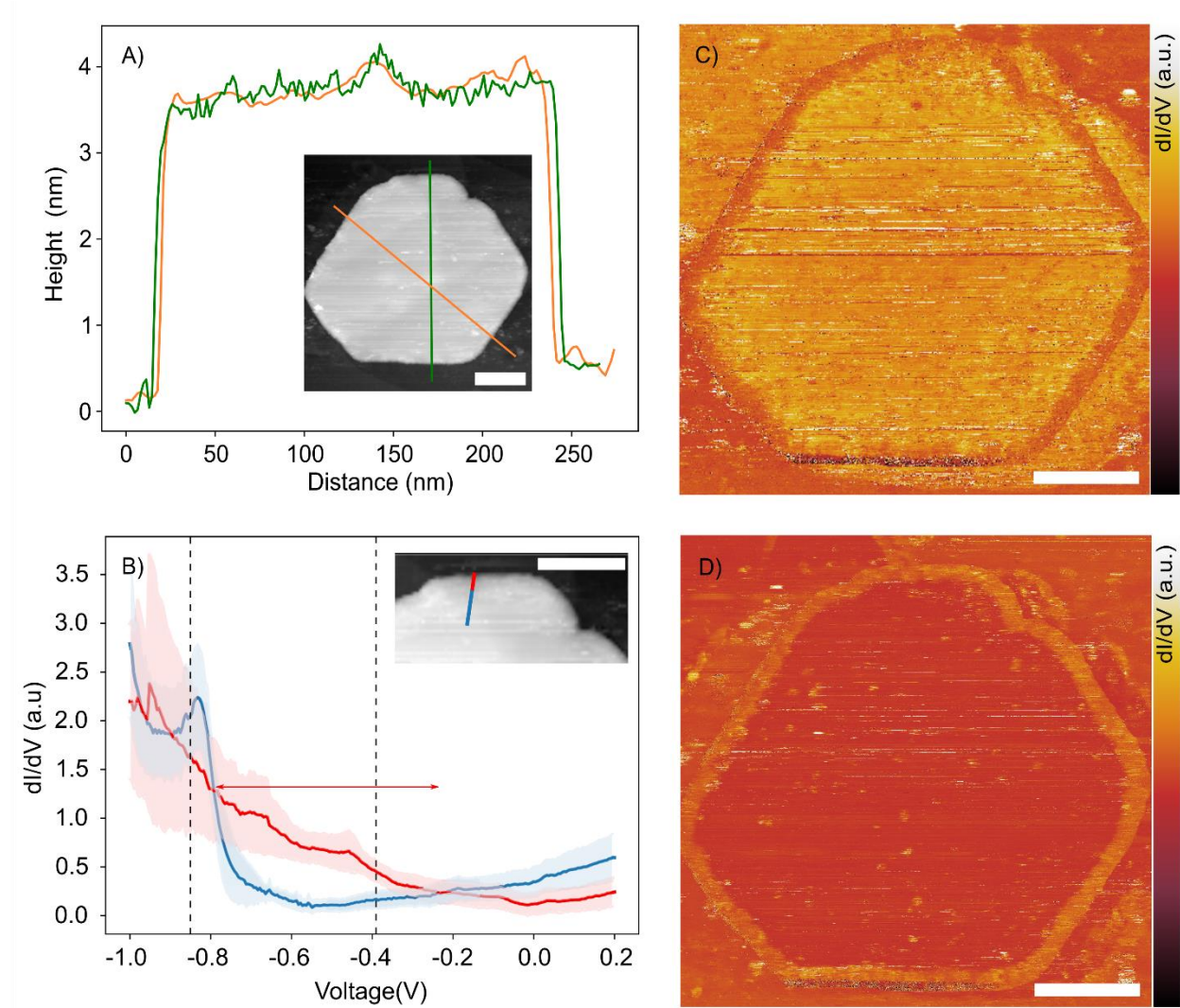
Figure 2. Characterization of the electronic states of a 4 QL thick Bi$_2$Se$_3$ platelet, in the interior and at the edge, with cryogenic scanning tunneling microscopy and spectroscopy.

(**A**) Height profile of a single platelet on a flat Au substrate along the orange and green lines shown in the inset. The diameter of the 2D sheet is about 230 nm. The height profile shows this Bi$_2$Se$_3$ platelet consists of 4 QLs. (**B**) Scanning tunneling spectrum of the local DOS(E,x,y) in the interior and at the edge. The blue curve shows the spectrum averaged over 7 positions on the blue line of

the inset, the standard deviation is presented as a blue gloom. Similar spectra taken in the center

of a platelet are presented in the SI, fig. S7. The red curve presents an average over 6 positions on

the red line, in which the standard deviation is presented as a red gloom. This spectrum represents

the edge state. The red arrow represents the energy region over which the density of states at the

edge is larger than in the interior. The set point in the spectroscopy is 1 nA. (**C**) LDOS(x,y) map

of the Bi_2Se_3 platelet acquired at a bias V of -0.85 V reflecting the top of the valence band. The

edge region is uniformly dark, reflecting a lower DOS(x, y) at this potential. (**D**) LDOS(x,y) map

of the Bi_2Se_3 platelet acquired at -0.39 V where the edge state is prominent. An 8-10 nm wide

band of high density of states follows the edge of the crystal, including the edge imperfections.

Scalebars are 50 nm. The set point in the maps is 0.5 nA.

Fig. 2A presents the height profile of a platelet of 3.6 nm in height, i.e., a homogeneous thickness

of 4 QLs, and a diameter of roughly 220 nm. The microscopic STM image (inset) shows that the

platelet has a hexagonal shape with some inclinations at the edge, see e.g. top left and right. We

took the absence of irregular and spiky spectroscopic data as a measure of cleanliness of the surface

of the Bi_2Se_3 crystal under investigation, as this led to reliable spectroscopic results in previous

investigations of wet-chemically prepared nanocrystals despite the lack of atomic resolved

microscopy(*26*). We found that the spectra at different positions in the interior area of the platelet

are all very similar, though with small quantitative differences. We therefore present position-

averaged spectra for each platelet. Interestingly, the spectra taken in the interior area differ strongly

from those taken in the last ~10 nm from the edge. This is illustrated by the blue and red curves

respectively in fig. 2B. The blue curve presents the dI/dV vs. V spectra averaged over 7 positions

on the blue line, typical for the DOS(E, x, y) in the interior area of the platelet. The standard

deviation around the average is presented as a blue gloom. The strong rise in the DOS(E, x, y) negative of -0.8 V reflects the high density of states corresponding to the valence bands, vide infra. Positive of -0.8 V, above the valence bands, the DOS(E,x,y) is small but nonzero, and it slowly rises again at energies above -0.2 V. This low but non-zero density of states can be attributed to the hybridized surface states (see below). Generally, the spectra near (but not at) the edge are very similar to spectra taken in the very center of the platelet, as illustrated in figure S10 for a 5QL platelet. Moreover, spectra measured on thin-film Bi_2Se_3 grown with precious gas phase methods(27-29) are very similar to our interior area spectra. This shows that our Bi_2Se_3 platelets are large enough for them to be considered as genuinely 2D, and that the absence of atomic resolution in our measurements does not impede the spectroscopic investigation of the band structure.

When the STM tip approaches the crystal edge closer than 10 nm, shown as the red line in the inset, we observe a sudden change in the spectra. The averaged spectrum of 6 positions on this red line is shown as the red spectrum in fig. 2B, with the standard deviation as a red gloom. Typically, we observe a lower DOS(E, x, y) in the energy region of the valence band (V < -0.85 V), but a higher DOS in a broad region between -0.85 V and -0.2 V, indicated with the red arrow. This is also evident from the DOS(x, y) maps presented in Fig. 2C,D. Panel C presents a map at -0.8 V over the entire crystal, illustrating a 8‑10 nm wide band of lower density of states following the circumference of the crystal. Conversely, in the energy region above the valence band (Fig. 2D) the situation is reversed with a 8‑10 nm wide band highlighting a larger density of states. This band follows the perimeter of the entire crystal, including the two edge inclinations at the upper right and left. The DOS map at the crystal edge is very smooth, i.e., without density fluctuations. Below, we will argue that if backscattering occurs, it would lead to density fluctuations on a length

scale around 10 nm, which would be clearly observable in the maps. The smooth appearance of the edge state in the DOS maps hence indicates that backscattering does not occur. A second example of a 4 QL crystal is presented in the SI, together with results on crystals with 1, 3, 5 and 6 QLs (figs. S5-S9). We find that Bi_2Se_3 platelets of 4-6 QLs show edge states very similar to those shown in Fig. 2 (see figs. S7, S8, S9). The platelets of 1 and 3 QLs in thickness show a density of states uniform over the entire platelet from the interior to the edge, demonstrating the absence of an edge state (figs. S5, S6).

Now, we argue that the edge states are not related to crystallographic disorder or a deviation in chemical composition. Our TEM analysis (Fig. 1 and figs. S1-S3) shows that the platelets are crystalline up to the last 1 nm region from the edge, where some disorder is visible. We also find that a combination of beam damage and annealing may cause removal of material at the edges in some NPLs (fig. S4). However, the edge states we observe are a factor 10 wider than the 1 nm disordered region present in as-synthesized platelets, and they are uniform in width along the entire crystal. Furthermore, figures 1 and S5-S9 show that the platelets on which we measured edge states have a uniform thickness. These are strong indications that crystal disorder cannot be related to the measured edge state. We also remark that all platelets are prepared with similar wet-chemical methods (see Materials and Methods) and have a similar crystallographic quality. In contrast, edge states are only observed for platelets of 4-6 QLs, which again indicates that the edge states are not due to crystallographic or chemical disorder.

In summary, we observe a well-defined edge state of about 8 nm in width for Bi_2Se_3 platelets of 4-6 QLs in thickness, while this edge state is absent in platelets of 1-3 QLs in thickness.
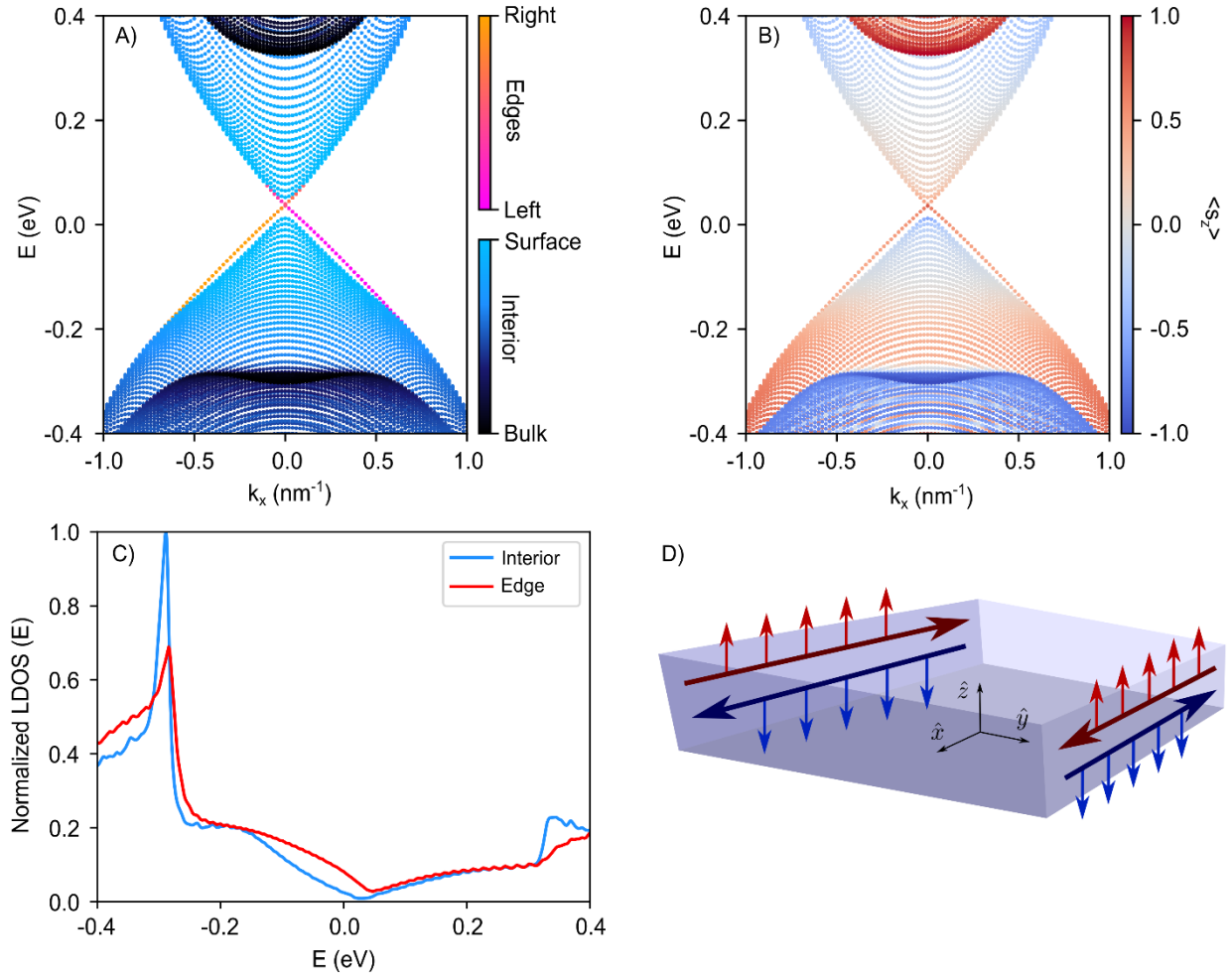
Figure 3. Theoretical analysis based on the low-energy eight-band $k\cdot p$ model for 2D Bi₂Se₃ ribbons, 4 QLs in thickness and 100 nm in width.

(**A**) Solution of the upper 4x4 branch provides one of the two helical edge states (red/orange). The states related to the inner QLs are in black, the (hybridized) top and bottom surface states in light blue. (**B**) Same solution as in A), but now presenting the spin-polarization $\langle s_z \rangle$ of the states, averaged over the z-direction (hence over 4 QL thickness). The Dirac line represents one state of the helical pair at the edge with an average spin polarization between 0.5 and 0.8 (in units of $\hbar/2$). The time-reversed state is presented in the SI, fig. S.12. (**C**) The resulting DOS for the ribbon of 4

QLs in thickness for the interior of the crystal (blue) and the edge (red). The edge state is discernable over a broad energy window, much broader than the inverted gap. (**D**) Scheme of the ribbon in real space with the calculated helical pair of edge states. The spin arrows reflect the projection on the z-axis (spin-polarization of $0.5\text{-}0.8$ (in units of $\hbar/2$)) of the spin, averaged over the thickness of the platelet. Each state is spatially extended over about 8 nm inside the ribbon and is present across the 4 QLs (see SI, fig. S13).

We have examined the nature of the observed state using theoretical models on two levels of complexity. First, we have adapted the low-energy model presented by Zhang *et al.*(*16*) to a more complete 8-band $\boldsymbol{k}\cdot\boldsymbol{p}$ model (Fig. 3 and figs. S11, S12), which allows us to calculate the Chern number per band and the $\mathbb{Z}_2$ invariant, see supplementary text. It predicts that infinite 2D crystals of 3,4, and 5 QLs are topologically non-trivial ($\mathbb{Z}_2 = 1$) and hence quantum spin Hall insulators, while crystals of 1,2 and 6 QLs are trivial. The 8-band model results in a Hamiltonian with two uncoupled and time-reversed 4-by-4 subspaces that we numerically solved. The solution for one sub-space for a ribbon with long dimensions in the x-direction, width L_y of 100 nm, and thickness (z-direction) of 4 QLs is shown in Fig. 3. The solution of the second subspace is simply the time-reversed version, presented in the SI, fig. S11. Fig. 3A shows the low-energy bands related to the two inner (black) and the outer (= surface, light blue) QLs. The Dirac line of the one-dimensional state at the edge is orange/red. Fig. 3B presents the spin component of all bands averaged over the z-direction (solution of one subspace). For the edge state, we find that the z-averaged spin component in the (x,y) crystal plane is zero, but there is a clear z- averaged spin-polarization of 0.5 to 0.8 (in units of $\hbar/2$) in the z-direction, locked to the momentum. Importantly, the solution of the other subspace (fig. S11) shows the time-inversed spin polarization of -0.5 to -0.8 expected

for the time reversed states. Both states together form the helical pair related to the predicted non-trivial topology for a Bi_2Se_3 crystal with 4 QLs. Fig. 3A,B shows that the one-dimensional edge state connects to the valence and conduction bands of the inner QLs via the outer QL surface states. The calculated (L)DOS is presented in Fig. 3C. The DOS(E) in the interior (blue) is comprised of the states of the inner and outer (surface) QLs, while the DOS(E) of the helical state at the edge is given in red. The DOS of the helical state is discernable over a relatively large energy region, although smaller than observed experimentally (see Fig. 2). Fig. 3D sketches the spatial characteristics of the helical edge state, with momentum and z-averaged spin. The state extends in depth across 4 QLs (fig. S13), and has a small width of about 9 nm, which is very similar to the experimental result. We remark that the state becomes wider close to the Dirac point, and a slight hybridization of the left and right states can be observed if the ribbon width becomes too small (<100 nm). To make use of the non-dissipative quantum channels in the most appropriate way in devices, the Fermi-level should therefore be distanced from the Dirac point.

We present a similar characterization of the band structure for a ribbon of 2 QLs in thickness in the SI, fig. S12. In this case, the bands are more strongly gapped and an edge state is absent (as $\mathbb{Z}_2$ = 0). The same holds for a ribbon of a single QL. For 6 QLs, the $\boldsymbol{k \cdot p}$ result also predicts $\mathbb{Z}_2 = 0$, in disagreement with the observation of an edge state. We should remark here that the calculated trivial gap is tiny and this disagreement should therefore be considered with care as the result is very sensitive to the bulk parameters used. Indeed, the first-principles theory (vide-infra) predicts $\mathbb{Z}_2 = 1$, in agreement with our experiment result.
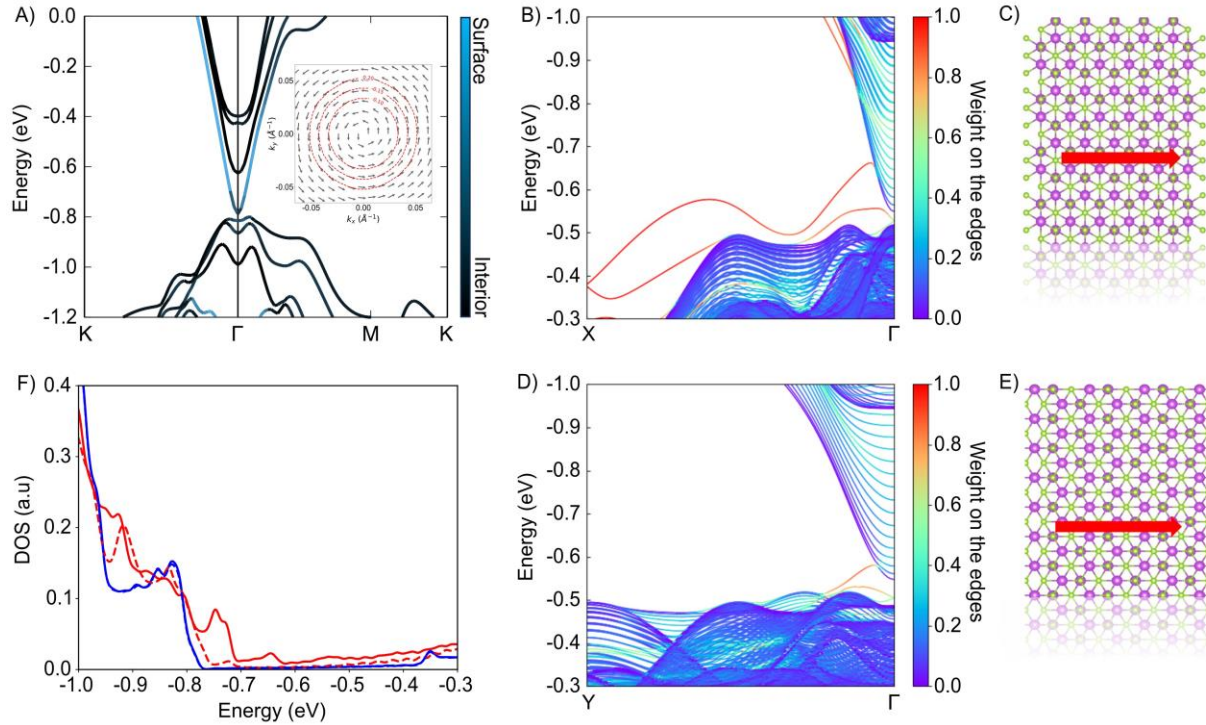
Figure 4. Theoretical analysis of the interior and surface states for a 2D infinite crystal, and edge states for 2D Bi₂Se₃ ribbons based on GW-TB calculations.

(**A**) Electronic band structure for an infinite 2D Bi_2Se_3 crystal, 4QLs in thickness, computed within the GW approximation. The atomic structure is fully relaxed using first-principles DFT calculations including spin-orbit coupling. Interior states are in black, surface states are in light blue. The inset shows the spin-momentum locking of one of the two lowest degenerate conduction bands (i.e. the blue surface state). The top of the valence band is set at -0.8 eV with respect to the Fermi-level. (**B,C**) Band structure along the Γ- X line for a 4 QLs ribbon of 36 nm in width. The ball-and-stick model shows the termination (zig-zag like) of the upper edge with the momentum for one of the helical states. Valence- and conduction bands are connected by an edge state (red) in line with $\mathbb{Z}_2 = 1$. (**D,E**) Similar, but now for a ribbon cut in the direction perpendicular to C. Valence- and conduction bands are connected by an edge state (red) in line with $\mathbb{Z}_2 = 1$. (**F**) The GW-TB calculated density of states in the interior of the ribbon (blue) with a peak corresponding to the top of the valence band (set at -0.8 eV with respect to the Fermi-level) and showing the

increasing density of states corresponding to the 4 lowest (doubly degenerate) conduction bands. Red-solid: density of states located at the edge with a zig-zag like termination, corresponding to panels B,C. Red-dashed: density of states at the edge corresponding to the ribbon in E. Note that the experimental edge state width (10 nm) is broader than the ball-and-stick schemes shown in C and E.

In addition to our 8-band $k \cdot p$ model, we used the GW approximation on top of first-principles density functional theory (DFT) to construct tight-binding (TB) models to calculate the band structure and DOS of infinite 2D Bi_2Se_3 crystals. The GW-TB parameters were then transferred, without change, to TB calculations for ribbons of varying widths up to 100 nm. For each thickness examined (1,2…6 QLs), the atomic structure of the Bi_2Se_3 crystal (atomic positions and cell) was thoroughly relaxed within the DFT framework, including spin-orbit coupling (see table S1). For each of the relaxed structures, the Kohn-Sham wavefunctions were projected onto maximally localized Wannier functions from which an atomistic TB Hamiltonian capturing many-body exchange and correlation effects for the 2D crystal was constructed. The GW band structures for infinite crystals with 3-6 QLs thickness are presented in Fig. S14. Although calculation of the $\mathbb{Z}_2$ invariant within the GW method is complicated due to the complex nature of the bands around Γ, we find that 2D Bi_2Se_3 with 1,2 and 3 QLs are trivial, while 4, 5 and 6 QLs are non-trivial, see table S2. Fig. 4A shows the GW band structure for an infinite 2D crystal with 4 QLs, which is in line with previous calculations*(30)* and with reported ARPES results(*21*). The bandgap is inverted and has a value of 58 meV (see table S3 for band gaps of Bi_2Se_3 slabs of different thickness). We remark that the lowest doubly degenerate conduction- and highest valence bands show spin-momentum locking (inset Fig. 4A), reminiscent of their protected character in the 3D case. In Figure 4B,D, we present the band structures for Bi_2Se_3 ribbons of 4 QLs in thickness and 36 nm

in width, with the infinite length in two orthogonal crystallographic directions resulting in a zig-zag like edge (Fig. 4C) or a straight edge (Fig. 4E). In both cases there is an edge state connecting the valence- to the conduction bands, in agreement with both the non-trivial $\mathbb{Z}_2$ invariant and the 8-band $\boldsymbol{k \cdot p}$ model. Thus, our calculations show the quantum spin Hall effect for a fully relaxed atomic structure. We remark here that small residual strain can result in a small gap opening in the edge state dispersion, a situation very close to a trivial/topological phase transition (figure S15). A similar situation has been previously reported, but remarkably, spin-momentum locking was still observed despite the gapping in the states(*31*). Lastly, Fig. 4F shows the density of states in the interior (blue) and at the edges (solid and dashed red lines). Here too, we observe a reasonable agreement with the experimental STS spectroscopy (Fig. 2 and SI figure S7).

Taking the results of the 8-band $\boldsymbol{k \cdot p}$ model for k-values between $0.2 - 0.5$ nm^{-1} (see Fig. 3) we expect, in case of impurity scattering, oscillatory patterns on a length scale roughly between 10 and 30 nm, while the first-principles theory (Fig. 4) predicts a length scale of $2.5 - 8.8$ nm. Hence, in case of backscattering, density-of-state oscillations on such length scales should be clearly observable in the platelets that we study. Indeed, such quasi-particle interference in thin crystals of Bi_2Se_3 has been observed, specifically for gapped surface states on step edges, see references *27* and *29*. In our measurements, however, we do not observe such patterns. A systematic study of backscattering due to a magnetic impurity in a one-dimensional topological edge state has been presented in ref. *32*. It must be noted that the absence of quasi-particle interference is not an absolute proof for the non-trivial character of the edge state, as other factors, such as a short coherence length, could play a role. We additionally observe that the measured edge state in our NPLs remains unchanged under an external magnetic field up to 1 Tesla (fig. S16, S17 and supporting text). Such resilience under an external field has been reported for other systems as

well (*33-40*). Furthermore, the predictions of a helical edge state by the 8-band $k\cdot p$ model and the ab-initio calculations provide a strong indication that the edge state that we observe in 2D Bi_2Se_3 platelets of 4,5 and 6 QLs is non-trivial.

The results presented here contribute to the understanding of the electronic topology in the evolution from a three to a two-dimensional system. Using the virtues of colloidal chemistry, self-standing (thus strain-free) two-dimensional crystals of Bi_2Se_3 with atomically precise thickness and finite lateral dimensions were prepared and characterized with cryogenic scanning probe spectroscopy complemented with a theoretical analysis. For Bi_2Se_3 crystals of 4-6 QLs in thickness, we observe a one-dimensional 8-10 nm wide channel at the crystal edge, absent in thinner crystals. We investigated the nature of this edge state with a continuum model and advanced ab-initio calculations. The resemblance between the theoretical predictions for 2D Bi_2Se_3 of 1-6 QLs in thickness and the results of scanning tunneling microscopy and spectroscopy experiments form a strong indication that the edge state that we observe is a helical quantum spin Hall state. We emphasize that, while our colloidal Bi_2Se_3 crystals provide an excellent model system for this fundamental study, growth from the gas phase combined with lithography will be required to create devices based on the quantum spin Hall effect.

ASSOCIATED CONTENT

Supporting Information.

The following files are available free of charge.

Associated content:

- Materials and Methods. Extended explanation on the synthesis procedure, characterization apparatus and modeling of the band structure using DFT and G_0W_0.
- Supplementary Text. Information on the effect of annealing on the NPLs, explanation on the extension of the four-band $\boldsymbol{k \cdot p}$ model into the eight-band $\boldsymbol{k \cdot p}$ model, and motivation for measurements under external magnetic field.

Supplementary figures:

- S1-S4: Characterization of the Bi_2Se_3 nanoplatelets using AFM, EDX and HAADF-STEM
- S5-S10: STM/STS data on Bi_2Se_3 nanoplatelets with thicknesses 1-6 QLs.
- S11-S13: Simulated data on 2QL and 4QL NPL using the 8-band $\boldsymbol{k \cdot p}$ model.
- S14: Band structures computed with DFT and GW
- S15: GW-TB calculations for an infinite crystal and a 2D (100 nm) ribbon.
- S16: STM/STS data on Bi_2Se_3 nanoplatelet (4QLs) subjected to a 1 T magnetic field.
- S17: STM/STS data on Bi_2Se_3 nanoplatelet (4 and 6QLs) subjected to a 0.5 T magnetic field.

Supplementary tables:

- S1: Simulated cell lattice parameters after geometric optimization using spin-orbit coupling.
- S2: Calculated $\mathbb{Z}_2$ invariants using DFT and G_0W_0 correction.
- S3: Calculated bandgaps for Bi_2Se_3 slabs of different thicknesses.

AUTHOR INFORMATION

Corresponding Author

*Corresponding author. Email: d.vanmaekelbergh@uu.nl

Author Contributions

The manuscript was written through contributions of all authors. All authors have given approval to the final version of the manuscript. †These authors contributed equally.

ABBREVIATIONS

NPL, nanoplatelet; STM/STS, scanning tunneling microscopy/scanning tunneling spectroscopy; 2D, two-dimensional; QSHI, quantum spin Hall insulator; QL, quintuple layer; (L)DOS, (local) density of states; TB, tight-binding; DFT, density functional theory; HAADF-STEM, high angle

annular dark field – scanning transmission electron microscopy; ARPES, angle resolved photo-emission spectroscopy; UHV, ultra-high vacuum.

REFERENCES

1. Talapin, D. V., Shevchenko, E. V. Introduction: Nanoparticle Chemistry. *Chem. Rev.* **116**, 10343-10345 (2016). DOI: 10.1021/acs.chemrev.6b00566

2. Hens, Z., De Roo, J. Atomically Precise Nanocrystals. *Journal of the American Chemical Society* **142**, 15627-15637 (2020). DOI: 10.1021/jacs.0c05082

3. Kovalenko, M. V. *et al.* Prospects of Nanoscience with Nanocrystals. *Acs Nano* **9**, 1012-1057 (2015). DOI: 10.1021/nn506223h

4. Park, Y. S., Lim, J. , Klimov, V. I. Asymmetrically strained quantum dots with non-fluctuating single-dot emission spectra and subthermal room-temperature linewidths. *Nat. Mater.* **18**, 249-255 (2019). DOI: 10.1038/s41563-018-0254-7

5. Lhuillier, E., Guyot-Sionnest, P. Recent Progresses in Mid Infrared Nanocrystal Optoelectronics. *IEEE J. Sel. Top. Quantum Electron.* **23,** 1-8 (2017). DOI: 10.1109/jstqe.2017.2690838

6. Knowles, K. E. *et al.* CuInS2/CdS nanocrystal phosphors for high-gain full-spectrum luminescent solar concentrators. *Chemical Communications* **51**, 9129-9132 (2015). DOI: 10.1039/c5cc02007g

7. Wu, K. F., Li, H. B., Klimov, V. I. Tandem luminescent solar concentrators based on engineered quantum dots. *Nat. Photonics* **12**, 105-110 (2018). DOI: 10.1038/s41566-017-0070-7

8. Hasan, M. Z., Kane, C. L. Colloquium: Topological insulators. *Reviews of Modern Physics* **82**, 3045-3067 (2010). DOI: 10.1103/RevModPhys.82.3045

9. Qi, X. L., Zhang, S. C. The quantum spin Hall effect and topological insulators. *Physics Today* **63**, 33-38 (2010). DOI: 10.1063/1.3293411

10. Fu, L., Kane, C. L. Superconducting proximity effect and Majorana fermions at the surface of a topological insulator. *Physical Review Letters* **100,** 096407 (2008). DOI: 10.1103/PhysRevLett.100.096407

11. Stanescu, T. D. *et al.* Proximity effect at the superconductor-topological insulator interface. *Physical Review B* **81**, 241210(R) (2010). DOI: 10.1103/PhysRevB.81.241310

12. Pribiag, V. S. *et al.* Edge-mode superconductivity in a two-dimensional topological insulator. *Nature Nanotechnology* **10**, 593-597 (2015). DOI: 10.1038/nnano.2015.86

13. Zareapour, P. *et al.* Proximity-induced high-temperature superconductivity in the topological insulators Bi2Se3 and Bi2Te3. *Nature Communications* **3,** 1056 (2012). DOI: 10.1038/ncomms2042

14. Alicea, J. Majorana fermions in a tunable semiconductor device. *Physical Review B* **81,** 125318 (2010). DOI: 10.1103/PhysRevB.81.125318

15. Kitaev, A. Anyons in an exactly solved model and beyond. *Annals of Physics* **321**, 2-111 (2006). DOI: 10.1016/j.aop.2005.10.005

16. Zhang, H. J. *et al.* Topological insulators in Bi2Se3, Bi2Te3 and Sb2Te3 with a single Dirac cone on the surface. *Nature Physics* **5**, 438-442 (2009). DOI: 10.1038/nphys1270

17. Yazyev, O. V., Moore, J. E., Louie, S. G. Spin Polarization and Transport of Surface States in the Topological Insulators Bi2Se3 and Bi2Te3 from First Principles. *Physical Review Letters* **105**, 266806 (2010). DOI: 10.1103/PhysRevLett.105.266806

18. Zhang, Y. *et al.* Crossover of the three-dimensional topological insulator Bi2Se3 to the two-dimensional limit. *Nature Physics* **6**, 584-588 (2010). DOI: 10.1038/nphys1689

19. Aguilera, I. *et al.* Many-body corrected tight-binding Hamiltonians for an accurates quasiparticle description of topological insulators of the Bi_2Se_3 family. *Physical review B,* **100,** 155147 (2019). DOI: 10.1103/PhysRevB.100.155147

20. Liu, C. X. *et al.* Oscillatory crossover from two-dimensional to three-dimensional topological insulators. *Physical Review B* **81,** 041307(R) (2010). DOI: 10.1103/PhysRevB.81.041307

21. Neupane, M. *et al.* Observation of quantum-tunnelling-modulated spin texture in ultrathin topological insulator Bi2Se3 films. *Nature Communications* **5**, 3841 (2014). DOI:10.1038/ncomms4841

22. Chiatti, O. *et al.* 2D layered transport properties from topological insulator Bi2Se3 single crystals and micro flakes. *Sci Rep* **6,** 27483 (2016). DOI: 10.1038/srep27483

23. Liu, Y. *et al.* Tuning Dirac states by strain in the topological insulator Bi_2Se_3. *Nature Physics.* **10,** 294-299 (2014). DOI: 10.1038/nphys2898

24. Zhang, J. *et al.* Raman Spectroscopy of Few-Quintuple Layer Topological Insulator Bi2Se3 Nanoplatelets. *Nano Letters* **11**, 2407-2414 (2011). DOI: 10.1021/nl200773n

25. Sun, Y. F. *et al.* Atomically Thick Bismuth Selenide Freestanding Single Layers Achieving Enhanced Thermoelectric Energy Harvesting. *Journal of the American Chemical Society* **134**, 20294-20297 (2012). DOI: 10.1021/ja3102049

26. Swart, I., Liljeroth, P., Vanmaekelbergh, D. Scanning probe microscopy and spectroscopy of colloidal semiconductor nanocrystals and assembled structures. *Chem. Rev.* **116**, 11181-11219 (2016). DOI: 10.1021/acs.chemrev.5b00678

27. Song, C *et al.* Probing Dirac Fermion Dynamics in Topological Insulator Bi_2Se_3 Films with a Scanning Tunneling Microscope. *Physical Review Letters.* **114**, 176602 (2015). DOI: 10.1103/PhysRevLett.114.176602

28. Wang, Y. *et al.* Scanning tunneling microscopy of interface properties of Bi_2Se_3 on FeSe. *Journal of physics: Condensed Matter.* **24**, 475604 (2012). DOI: 10.1088/0953-8984/24/47/475604

29. Zhang, T. *et al.* Scanning tunneling microscopy of gate tunable topological insulator Bi_2Se_3 thin films. *Physical Review B.* **87.** 115410 (2013). DOI: 10.1103/PhysRevB.87.115410

30. Förster, T. *et al.* Two-dimensional topological phases and electronic spectrum of Bi_2Se_3 thin films from *GW* calculations. *Physical review B.* **92,** 201404(R) (2015). DOI: 10.1103/PhysRevB.92.201404

31. Xu, SY. *et al.* Unconventional transformation of spin Dirac phase across topological quantum phase transition. *Nature Communications.* **6**, 6870 (2015). DOI: 10.1038/ncomms7870

32. Jäck, B. *et al.* Observation of backscattering induced by magnetism in a topological edge state. *Proceedings of the National Academy of Sciences.* **117,** 16214 (2020). DOI: 10.1073/pnas.2005071117

33. Zhang, S. B., Zhang, Y. Y., Shen, S. Q. Robustness of quantum spin Hall effect in an external magnetic field. *Physical Review B* **90,** 115305 (2014). DOI: 10.1103/PhysRevB.90.115305

34. Skolasinski, R. *et al.* Robust helical edge transport in quantum spin Hall quantum wells. *Physical Review B* **98,** 201404(R) (2018). DOI: 10.1103/PhysRevB.98.201404

35. Tkachov, G., Hankiewicz, E. M. Ballistic Quantum Spin Hall State and Enhanced Edge Backscattering in Strong Magnetic Fields. *Physical Review Letters* **104,** 166803 (2010). DOI: 10.1103/PhysRevLett.104.166803

36. Goldman, N., Beugeling, W., Smith, C. M. Topological phase transitions between chiral and helical spin textures in a lattice with spin-orbit coupling and a magnetic field. *Epl* **97,** 23003 (2012). DOI: 10.1209/0295-5075/97/23003

37. Knez, I., Du, R. R., Sullivan, G. Evidence for Helical Edge Modes in Inverted InAs/GaSb Quantum Wells. *Physical Review Letters* 107, 136603 (2011). DOI: 10.1103/PhysRevLett.107.136603

38. Knez, I. *et al.* Observation of Edge Transport in the Disordered Regime of Topologically Insulating InAs/GaSb Quantum Wells. *Physical Review Letters* 112, 026602 (2014). DOI: 10.1103/PhysRevLett.112.026602

39. Wang, Q., Sheng, L. Edge mode of InAs/GaSb quantum spin hall insulator in magnetic field. *Acta Phys. Sin.* **64,** 097302 (2015). DOI: 10.7498/aps.64.097302

40. Du, L. J. *et al.* Robust Helical Edge Transport in Gated InAs/GaSb Bilayers. *Physical Review Letters* **114,** 096802 (2015). DOI: 10.1103/PhysRevLett.114.096802

41. Li, C. *et al.* A simple method to clean ligand contamination on TEM grids. *Ultramicroscopy,* **221**, 113195 (2021). DOI: 10.1016/j.ultramic.2020.113195

42. Giannozzi, P. *et al.* QUANTUM ESPRESSO: a modular and open-source software project for quantum simulations of materials. *Journal of Physics: Condensed Matter* **21**, 395502 (2009). DOI: 10.1088/0953-8984/21/39/395502

43. Van Setten, M.J. *et al.* The PseudoDojo: Training and grading a 85 element optimized norm-conserving pseudopotential table, *Computer Physics Communication* **226**, 39-54 (2018). DOI: 10.1016/j.cpc.2018.01.012

44. Perdew, J.P., Burke, K., Enzerhof, M. Generalized Gradient Approximation Made Simple, *Physics Review Letters* **78,** 3865-3868 (1996), DOI: 10.1103/PhysRevLett.77.3865

45. Sangalli, D. *et al.* Many-body perturbation theory calculations using the yambo code, *Journal of Physics: Condensed Matter* **31,** 325902 (2019), DOI: 10.1088/1361-648X/ab15d0

46. Pizzi, G. *et al.* Wannier90 as a community code: new features and applications, *Journal of Physics: Condensed Matter* **32**, 165902 (2020). DOI: 10.1088/1361-648X/ab51ff

47. Wu, QS. *et al.* WannierTools: An open-source software package for novel topological materials, *Computer Physics Communications* 224, 405-416 (2018) DOI: 10.1016/j.cpc.2017.09.033

48. Lu, H. Z. *et al.* Massive Dirac fermions and spin physics in an ultrathin film of topological insulator. *Physical Review B* **81**(11), 115407 (2010). DOI: 10.1103/PhysRevB.81.115407

49. Shan, W. Y., Lu, H. Z., Shen, S. Q. Effective continuous model for surface states and thin films of three-dimensional topological insulators. *New Journal of Physics* **12**(4), 043048 (2010). DOI: 10.1088/1367-2630/12/4/043048

50. Kane, C. L., Mele, E. J. Quantum spin Hall effect in graphene. *Physical Review Letters*, **95**(22), 226801 (2005). DOI: 10.1103/PhysRevLett.95.226801

51. Fu, L., Kane, C.L. Topological insulators with inversion symmetry. *Physical Review B* **76**(4), 045302, (2007). DOI: 10.1103/PhysRevB.76.045302

52. Kane, C. L., Mele, E. J. Z(2) topological order and the quantum spin Hall effect. *Physical Review Letters* **95,** 146802 (2005). DOI: 10.1103/PhysRevLett.95.146802

53. Nayak, A. K. *et al*. Resolving the topological classification of bismuth with topological defects. *Science advances* **5**(11), eaax6996 (2019). DOI: 10.1126/sciadv.aax6996

BRIEFS.

By measuring the density of states of individual Bi_2Se_3 nanoplatelets, each with finite lateral dimensions and a precise number of quintuple layers (1-6), we image and characterize an 8-10 nm wide, one-dimensional quantum state that follows the entire edge of the crystal, provided that the thickness of the crystal is 4, 5 or 6 quintuple layers.
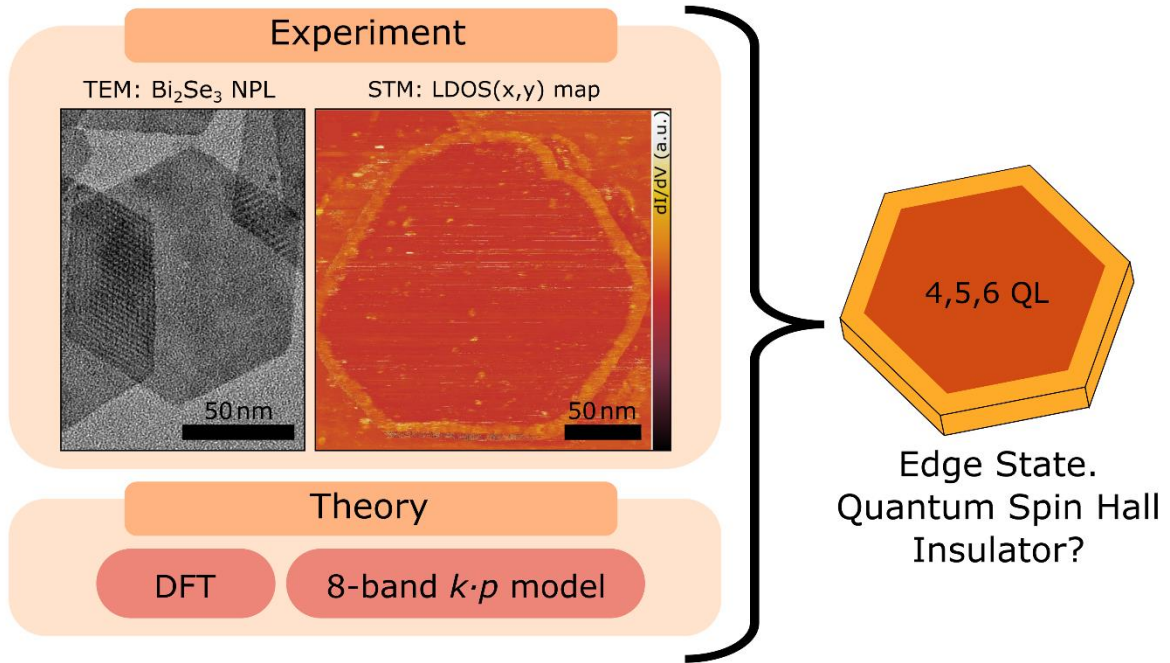
Figure X: For Table of Contents Only.